Chapter 2
Electron–Phonon and Exciton–Phonon Coupling in Light Harvesting, Insights from Line-Narrowing Spectroscopies

Jörg Pieper and Arvi Freiberg

Abstract In photosynthetic antenna complexes, apart from defining the positions and orientations of the pigment molecules, the protein matrix plays an important role in excitation energy transfer dynamics. The low-frequency protein vibrations—often referred to as phonons—serve as acceptor modes in nonadiabatic excitation energy transfer between energetically inequivalent electronic or excitonic energy states, assuring a spatially and energetically directed flow of excitation energy within an antenna complex. Due to electron–phonon and electron–vibrational coupling, the purely electronic or excitonic transitions of pigment molecules are usually accompanied by a broad and asymmetric low-frequency sideband spreading a few hundred wavenumbers and, in addition, by a number of distinct lines covering the frequency range between ~200 and 1,700 cm^{-1}. The low-frequency sideband peaking at 20–30 cm^{-1} is typically identified with a continuous distribution of widely delocalized protein vibrations. The narrow lines at higher frequencies can mostly be attributed to localized pigment vibrations of (bacterio-) chlorophyll molecules, which are only slightly modified by the surrounding protein matrix. In conventional absorption or fluorescence spectra measured at cryogenic temperatures this substructure is usually hidden by significant inhomogeneous broadening due to the heterogeneity of the amorphous protein matrix. Line-narrowing spectroscopies like spectral hole burning and (difference) fluorescence line-narrowing have been proved to be powerful experimental tools for unraveling the hidden homogeneous spectral features from the inhomogeneously broadened spectra. This contribution focuses on electron–phonon

J. Pieper (✉)
Institute of Physics, University of Tartu, Ravila 14c, 50411 Tartu, Estonia
e-mail: pieper@ut.ee

A. Freiberg
Institute of Physics, University of Tartu, Ravila 14c, 50411 Tartu, Estonia

Institute of Molecular and Cell Biology, University of Tartu, Riia 23, 51010 Tartu, Estonia
e-mail: arvi.freiberg@ut.ee

J. Golbeck and A. van der Est (eds.), *The Biophysics of Photosynthesis*,
Biophysics for the Life Sciences 11, DOI 10.1007/978-1-4939-1148-6_2,
© Springer Science+Business Media New York 2014

and exciton–phonon coupling in photosynthetic pigment–protein complexes. It also discusses the underlying concepts of electron–phonon and electron–vibrational coupling starting from the Franck–Condon principle and the general composition of homogeneously and inhomogeneously broadened spectra of pigment–protein complexes. The advantages and limitations of different spectroscopic techniques in revealing the electron–phonon and electron–vibrational coupling parameters are discussed based on model calculations. The chapter concludes with a discussion of recent results on electron–phonon and electron–vibrational coupling for isolated (bacterio-) chlorophyll molecules as well as for selected photosynthetic pigment–protein complexes.

Keywords Photosynthesis • Pigment–protein complex • Electron–phonon coupling • Electron–vibrational coupling • Huang–Rhys factor • Spectral density • Spectral hole burning • Fluorescence line-narrowing

Abbreviations

BChl	Bacteriochlorophyll
Chl	Chlorophyll
FLN	Fluorescence line narrowing
FWHM	Full-width-at-half-maximum
IDF	Inhomogeneous distribution function
LH1	Light harvesting complex 1 (of purple bacteria)
LH2	Light harvesting complex 2 (of purple bacteria)
LHC II	Light harvesting complex II (of green plants)
PSB	Phonon sideband
SHB	Spectral hole burning
SMS	Single-molecule spectroscopy
ZPL	Zero-phonon line

2.1 Introduction

For efficient light-harvesting nature has developed specialized pigment–protein complexes referred to as “antennae” whose electronic absorption spectra span broad energy ranges of several hundreds to two thousand wavenumbers and are well adapted to the maximum of the solar radiation reaching the earth’s surface. Since in many cases photosynthetic antenna complexes consist of arrays of closely spaced pigment molecules, excitonic interactions have to be taken into account (see Sect. 1.1). The exciton, a bound state of an electron and a hole, is regarded as an elementary excitation of condensed matter that can transfer energy without transporting net electric charge. Relevant for photosynthesis are short range Frenkel excitons where an electron and a hole reside on the same molecule and propagate

together [1]. Excitons in the context of photosynthesis have already been discussed since 1938 [2]; a modern overview of photosynthetic excitons can be found in [3]. Within the recent years, much effort has been invested to unravel the excitonic energy level structure and excitation energy transfer dynamics in photosynthetic antenna complexes as well as the underlying pigment–pigment and pigment–protein interactions (see Sects. 1.1 and 1.2) by different experimental approaches like time-resolved spectroscopy [4], spectrally selective techniques [5] or single-molecule spectroscopy (SMS) [6], and more recently, by two-dimensional electronic spectroscopy [7]. The wealth of experimental information has initiated detailed theoretical simulations of excitation energy transfer, specifically, in the major antenna complexes LHC II of green plants (see, e.g., Müh et al. [8] and references therein) and LH2 from purple bacteria (see, e.g., Novoderezhkin and van Grondelle [9], Freiberg and Trinkunas [10]).

In addition to the pigment–pigment interactions discussed above, photosynthetic antenna complexes are also characterized by electron–vibrational coupling, which refers to the interaction between a molecular electronic transition and intramolecular nuclear vibrations determining the vibronic structure of optical spectra of individual pigments (chromophores) [11]. A special case of electron–vibrational coupling is the chromophore–host interaction, which gives rise to the electron–phonon structure of the spectra. Strictly speaking, phonons are collective vibrational modes (standing waves) in perfectly periodic lattices, in which all the lattice particles simultaneously participate. Here, the term phonon is more loosely used to distinguish delocalized low-frequency protein vibrations in pigment–protein complexes (and amorphous lattices in general) from the higher-frequency intramolecular vibrations localized on the (bacterio)chlorophyll ((B)Chl) and other pigment molecules bound to the photosynthetic antenna complex. The electron–phonon and electron–vibrational (vibronic) interactions together shape the so-called homogeneously broadened spectra of the photosynthetic pigment molecules surrounded by an optically transparent dielectric medium, here consisting of the native protein scaffold and buffer solution. In case of non-negligible excitonic coupling between the pigment molecules of a given photosynthetic complex, one has to refer to exciton–phonon coupling. In either regime, the purely electronic/excitonic transitions of photosynthetic pigments embedded into amorphous protein environments are thus typically accompanied by a large number of vibrational replicas due to electron–phonon and vibronic coupling. The energetic difference between the purely electronic/excitonic origin and a given vibrational line generally reflects the corresponding vibrational frequency.

This is illustrated in Fig. 2.1 by showing vibrational spectra of the ground state of a Chl*a*-containing water soluble chlorophyll-protein (Chl*a*-WSCP) complex [12], obtained by spectrally selective low-temperature difference fluorescence line-narrowing technique at 4.5 K (delta-FLN, see below). The Chl*a*-WSCP complex is well suited for studies of pigment–pigment and pigment–protein interactions, because it binds only two Chl*a* molecules, which are excitonically coupled with moderate interaction energy of roughly ~100 cm^{-1}, and which in the simplest approximation [13] form only two excitonic energy levels denoted by E_1^+ and E_1^-.

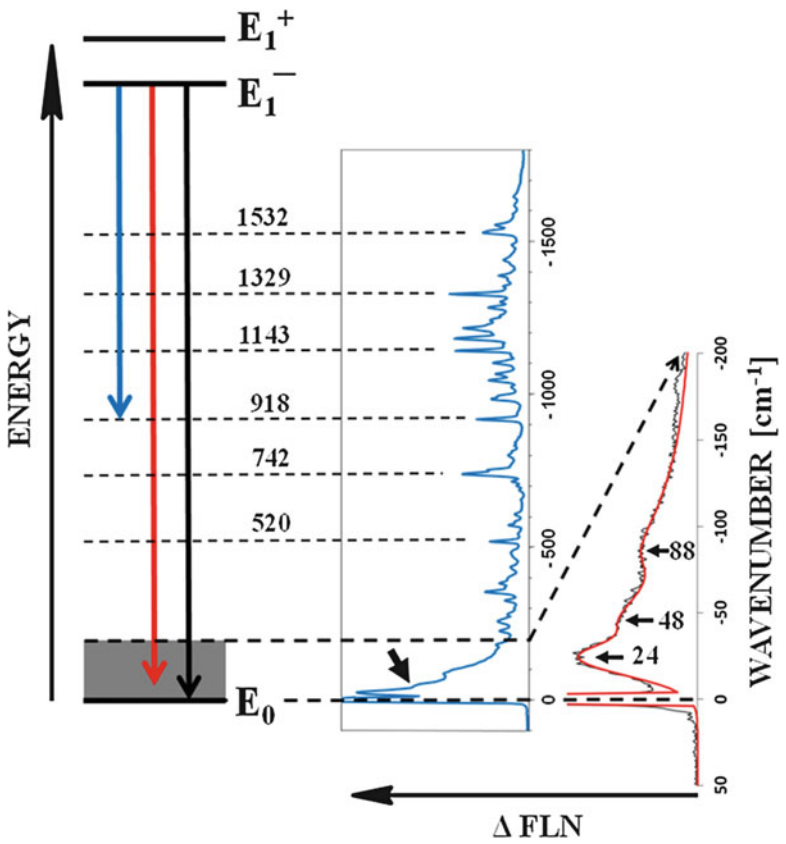


Fig. 2.1 Schematic vibrational energy level diagram of Chl*a*-WSCP derived from high-resolution delta-FLN spectroscopy at 4.5 K. A 4.5 K delta-FLN spectrum of Chl*a*-WSCP is shown as a *blue line*; selected vibronic lines are labeled by their frequencies in wavenumbers (data taken from [12]). The ZPL is cut off for clarity. A magnification of the phonon region (labeled by a *thick black arrow*) is shown to the right (*black noisy line*); the magnified wavenumber region is indicated by a *dashed arrow*. The peaks in the phonon sideband are also labeled by their frequencies. A simulation of the phonon region (*red line*) is calculated using a Huang–Rhys factor S of 0.81 and three one-phonon profiles with peak frequencies of 24, 48, and 88 cm^{-1}, respectively. In the energy level diagram (see *left* side), the ground state as well as lower and higher exciton level of Chl*a*-WSCP are given by thick black lines and labeled by E_0, E_1^-, and E_1^+, respectively. The ground state ($E_1^- \rightarrow E_0$) vibrational levels are indicated by *dashed lines*, the phonon region by *grey color*. The *black arrow* represents a zero-phonon (purely excitonic) transition, while the *blue* and *red arrows* correspond to transitions involving Chla vibrations and phonons, respectively

The delta-FLN spectrum shown in the center of Fig. 2.1 generally consists of three parts: (1) the intense and narrow purely excitonic line at the excitation frequency of $\omega = (E_1 — E_0)/\hbar$. As follows, this frequency is for convenience taken as zero point and considered as an origin of the delta-FLN spectrum. The readers familiar with many spectroscopic techniques might recognize the analogy with Raman

spectroscopy (see, e.g., Aartsma and Matysik [4]); (2) a broad, asymmetric phonon sideband adjacent to the purely excitonic line on its low-energy side and spreading up to ~200 cm^{-1}; and (3) around 50 distinct vibrational lines covering the frequency range between ~200 and 1,700 cm^{-1}. The phonon sideband peaking at ~24 cm^{-1} is shown in more detail in the rightmost spectrum of Fig. 2.1. It is typically identified with a broad and continuous distribution of widely delocalized low-frequency protein vibrations and their multi-quantum transitions, while the narrow vibrational lines at frequencies higher than ~200 cm^{-1} can mostly be attributed to localized Chl*a* vibrations, only slightly modified by the environment (see Rebane [11] and Kühn et al. [14] for reviews). Since the coupling between the excitonic transition and the intramolecular vibrational degrees of freedom is weak [12], the vibrational replicas represent in a good approximation just single-quantum transitions for the local vibrational modes of Chl*a*. Figure 2.1 also shows a schematic energy level diagram of the ground state $E_1^- \rightarrow E_0$ phonon and vibrational transitions indicated by grey color and dashed lines, respectively. The black arrow represents a zero-phonon (purely excitonic) transition, while the blue and red arrows correspond to transitions involving Chl*a* vibrations and phonons, respectively. The complementary excited state vibrational frequencies can be observed in hole burned spectra at 4.5 K and typically show little variation [15].

It is apparent from Fig. 2.1 that even the spectrum of a simplest pigment–protein complex is rather complicated and extends over a significant range of frequencies. Therefore, detailed knowledge of the parameters of electron–phonon and electron–vibrational coupling is essential for a proper understanding and theoretical simulations of optical spectra as well as energy transfer rates in photosynthetic systems. Furthermore, the example of WSCP underlines that photosynthetic pigment–protein complexes often feature excitonic rather than localized electronic states, so that exciton–phonon and exciton–vibrational couplings also have to be considered (see below). The rich vibrational structure characteristic for homogeneously broadened spectra is, however, not apparent in conventional absorption and fluorescence spectra even at low temperatures, which are widely structureless due to significant heterogeneity of the pigment microenvironments and ensemble averaging, as will be discussed in some detail below. This observation constitutes the need for experimental techniques which are capable of revealing phonon and vibrational substructures at least at low temperatures such as spectral hole burning (SHB) [16, 17], FLN [18], and delta-FLN [19–21]. In principle, the low-temperature SMS [6, 22, 23] also belongs to this list. However, as is well known, the single-molecule spectra suffer from poor signal to noise ratio, rendering investigation of weak vibronic and phonon structures a rather difficult task. Therefore, in the present chapter we will limit ourselves to providing an overview on the analysis of phonon structure in line-narrowed (SHB, FLN, delta-FLN) optical spectra. Electron–vibrational coupling will be addressed in parallel, because of the many analogies to the case of phonons.

The present chapter is organized as follows: In Sect. 2.2 we will introduce the homogeneous lineshape of an isolated pigment molecule embedded into a protein matrix and explain the origin of the electron–phonon and electron–vibrational

coupling. The meaning of the frequently used terms in the corresponding literature, such as the Huang–Rhys factor and reorganization energy, will be clarified. Effects of excitonic coupling on the electron–phonon coupling parameters will be shortly commented. In Sect. 2.3 we will follow with a discussion of the origin of inhomogeneous spectral broadening and its effect on conventional absorption and fluorescence spectra. In Sect. 2.4 the different types of line-narrowing spectroscopies (SHB, FLN, and delta-FLN) will be introduced. Their similarities and differences will be illustrated by model calculations. Finally, in Sect. 2.5, we will provide a short overview and critical discussion of some experimental results related to electron/exciton–phonon and electron/exciton–vibrational coupling for (B)Chl*a* pigment molecules either in isolation or when embedded into the major photosynthetic light-harvesting complexes of green plants (LHC II) and purple bacteria (LH2).

2.2 Conceptual Basis of Electron–Phonon and Electron–Vibrational Coupling: Homogeneously Broadened Spectra

A quantitative description of electron–phonon coupling requires a number of simplifying assumptions to be made about the complex macromolecular pigment–protein system, including the adiabatic, harmonic, and Franck–Condon approximations (see Rebane [11] and references therein). For simplicity, the theory of electron–phonon coupling discussed below is strictly valid for highly localized electronic transitions only, e.g., for isolated (B)Chl molecules at large distance from other chromophores in a given photosynthetic complex. A short overview of the excitonic coupling effects is provided at the end of this Section.

Within the adiabatic approach, the motions of the heavy nuclei of a macromolecule are assumed to be uncorrelated with the faster motions of the much lighter electrons so that the two types of motions can be separated. This assumption is the prerequisite for the description of a macromolecule in terms of a potential energy diagram as shown in Fig. 2.2 depicting the motion of the system of heavy nuclei along one selected conformational coordinate q_k for each the two electronic states E_i and E_f. More generally, a macromolecular system of N atoms is characterized by 3N motional degrees of freedom including three translational and three rotational components so that we arrive at a total of 3N-6 vibrational eigenmodes characterized by their eigenfrequencies ω_k. A realistic assumption for E_i is a Lennard-Jones potential [11] with an attractive and a repulsive component at large and small values of the conformational coordinate, respectively. In thermal equilibrium at low temperature, however, one can assume that the nuclei perform only small fluctuations around the respective potential energy minima. Within the harmonic approximation, it is then presumed that these fluctuations can be described by parabolic potentials, i.e., the motion of the nuclei along one conformational coordinate is equivalent to that of a harmonic oscillator moving around an equilibrium position.

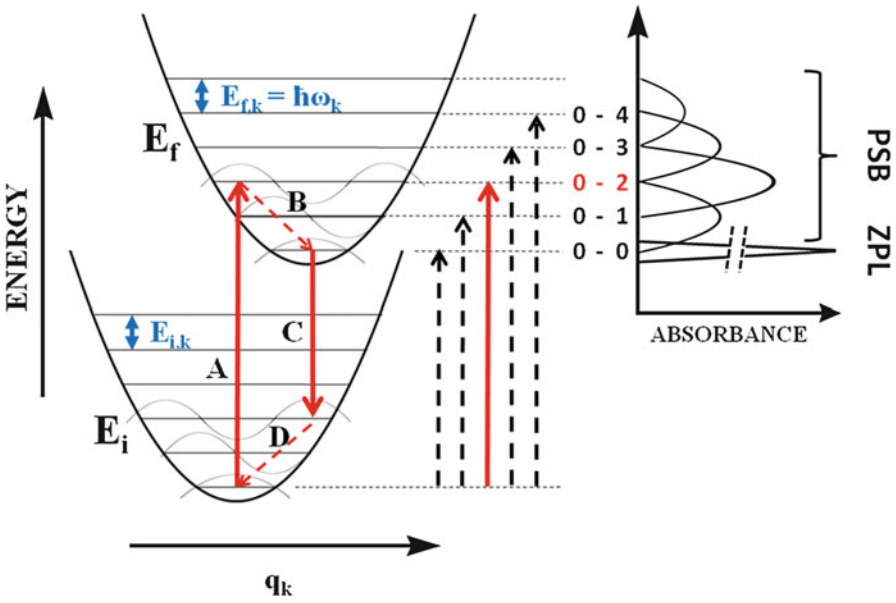


Fig. 2.2 Schematic potential energy diagram of a pigment embedded into an amorphous protein matrix for the case of linear harmonic Franck–Condon coupling (*left side*) and the corresponding absorption spectrum (*right side*) in the low temperature limit where k_BT is much smaller than the vibrational energy $\hbar\omega_k$ of the considered nuclear motion. The potential energy curves of a selected nuclear motion are plotted as a function of its conformational coordinate q_k in the electronic ground and excited states E_i and E_f, respectively. The most probable transitions are given by *red full arrows* for the cases of absorption (A) and fluorescence (C). Schematic vibronic wavefunctions are given by grey lines for selected vibrational energy levels to illustrate the principle of the overlap integral in Eq. (2.1). *Red dashed arrows* (B, D) indicate fast vibrational relaxation following the initial electronic transition. The energy level diagram to the right of the potential energy curves illustrates the different (multi-) quantum transitions of the selected vibrational frequency ω_k in absorption. The corresponding spectral features are qualitatively shown in the right diagram, where 0–0 transitions constitute the ZPL (not in scale) and all transitions involving phonons (0–1, 0–2, etc.) constitute the PSB. Note that in contrast to the different quantum transitions of a single vibrational frequency ω_k shown here, the vibronic energy levels depicted in Fig. 2.1 correspond to one-quantum transitions of different vibrational eigenfrequencies

The various harmonic oscillators characterized by a frequency ω_k and the corresponding discrete energy levels with an energetic spacing of $\hbar\omega_k$ (as shown in Fig. 2.2) are independent from each other. Upon electronic excitation due to absorption of a light quantum the system of nuclei generally undergoes a rearrangement leading to a shift of the equilibrium position and change of curvature of the harmonic potential in the excited electronic state E_f. These changes determine the Franck–Condon type of vibronic coupling [24, 25]. As a first approximation, however, the parabolic potentials in the ground and the excited electronic state are usually taken identical, except for the shift of the equilibrium position, resulting in an identical phonon frequency ω_k in both electronic states [11]. This is the

situation also illustrated by the shifted potentials E_i and E_f of the ground and excited electronic states shown in Fig. 2.2.

The transition probabilities between a given vibrational level in the electronic ground state and any vibrational level in the excited electronic state as shown in Fig. 2.2 are given by the Franck–Condon principle. Within the classical Franck–Condon approach, the heavy nuclei do not react during a fast electronic transition upon light absorption, i.e., the latter transition is vertical in the potential energy diagram shown in Fig. 2.2. A detailed quantum mechanical description is beyond the scope of this contribution; a comprehensive derivation can be found in [11]. Briefly, the transition probability between the vibrational levels n and m in the initial and the final electronic states E_i and E_f, respectively, is given by the square of the product of electronic transition probability $D_{f,i}$ and the overlap integral of the respective vibrational wave functions of each oscillator k [11]

$$W_{fm,in} = \left| D_{f,i} \prod_k \langle m_k | n_k \rangle \right|^2 . \tag{2.1}$$

Equation (2.1) is at the heart of the electron–phonon and electron–vibrational coupling. Strictly speaking, the electronic transitions between the initial and final electronic states are almost always coupled to the vibrations and the quantum mechanical formulation of the Franck–Condon principle provides a probability for each vibrational transition coupled to an optical excitation by evaluation of the overlap integral in Eq. (2.1). As an illustration, schematic wavefunctions are shown for selected vibrational levels in Fig. 2.2. For brevity, we will consider here only the case of sufficiently low temperatures, i.e., at $k_B T \ll \hbar\omega_k$, where k_B is the Boltzmann constant. In this case only the lowest vibrational level of the electronic ground state is thermally populated and serves as the starting point of an electronic transition in absorption. Generally, the final vibrational level in the excited electronic state depends on the shift of the equilibrium position of the harmonic potential in the excited electronic state. The situation depicted in Fig. 2.2 shows the largest overlap of ground and excited state wavefunctions in case of a transition from the lowest vibrational level in the electronic ground state E_i to the second vibrational level in the excited electronic state E_f, i.e., the absorption process leads to creation of two vibrational quanta or phonons and thus requires higher light energy than the purely electronic or zero-phonon transition. Therefore, the schematic absorption spectrum on the right side of Fig. 2.2 exhibits the most intense feature at the position of the two-quantum/two-phonon (0–2) transition. All other quantum transitions shown are less probable and appear with smaller intensity. We distinguish transitions with and without participation of the vibrational quanta/phonons that form the phonon sideband (PSB) and the zero-phonon line (ZPL), respectively, as also shown in Fig. 2.2. The reason for the different linewidths of ZPL and PSB components is discussed below. Following light absorption, the macromolecular system depicted in Fig. 2.2 is in nonequilibrium state (again assuming that $k_B T \ll \hbar\omega_k$), so that it subsequently relaxes to the lowest vibrational

level in the excited electronic state E_f (see dashed arrow labeled with B). The energy released upon this nonradiative equilibration process is called the reorganization energy. Then, following the Franck–Condon principle, de-excitation occurs via a radiative transition into the second vibrational level of the electronic ground state E_i, again followed by vibrational relaxation into the ground state in thermal equilibrium (dashed arrow labeled with D). In contrast to absorption, the average light quantum emitted as fluorescence is smaller than that of a zero-phonon transition, so that in this simple case the electron–phonon coupling leads to mirror symmetry between the absorption and fluorescence transition probabilities/spectra. The energetic difference between the absorption and fluorescence spectral maxima is called Stokes shift; it is numerically equal to twice the reorganization energy (see Eq. (2.7) below). Qualitatively, the above potential energy model applies to both localized vibrations of (B)Chl molecules and delocalized protein vibrations (phonons).

The complexities rapidly amount in the more general cases of arbitrary potential surfaces in the ground and excited electronic state, and especially, when the electronic transition probability $D_{f,i}$ in Eq. (2.1) depends on nuclear coordinates resulting in a breakdown of mirror symmetry [24, 25]. This latter effect in relation with the Chl*a* and BChl*a* spectra will be discussed in the last part of this chapter. At higher temperatures with $k_BT \ll \hbar\omega_k$, thermal population of higher vibrational levels has to be considered so that transitions with annihilation of vibrations/phonons become available. This generally leads to a redistribution of the electron–vibrational band intensity in favor of the PSB. Also, in absorption, the PSB components at the low-energy side of the ZPL are observed, in addition to those present at the high-energy side. The latter and former are referred to as Stokes and anti-Stokes parts of the PSB [11, 26].

We will now discuss the spectral lineshape of an isolated pigment molecule whose electronic transition is coupled to a distribution of delocalized protein phonons as well as to intramolecular localized vibrations. As discussed above, this spectrum consists of a narrow purely electronic ZPL, a broad PSB, and a series of narrow vibrational lines lying towards higher energy in absorption (see red line in Frame A of Fig. 2.3, where for clarity only the ZPL and PSB parts are reproduced). We assume that the shape of the latter spectrum is the same for all chemically equivalent molecules in a bulk sample, so that it can be referred to as the homogeneously broadened single site absorption spectrum. Furthermore, as is frequently done, we apply a "mean frequency approximation" for phonons, i.e., the distribution of 3N-6 eigenmodes of the protein shall be represented by a single band of mean frequency ω_m and a lineshape that accounts for the whole ensemble of energetically closely spaced protein vibrations. The analytical expression for the low-temperature single site absorption and fluorescence spectra of a chromophore embedded into an amorphous protein matrix within the approximation of Eq. (2.1) is given by [27]

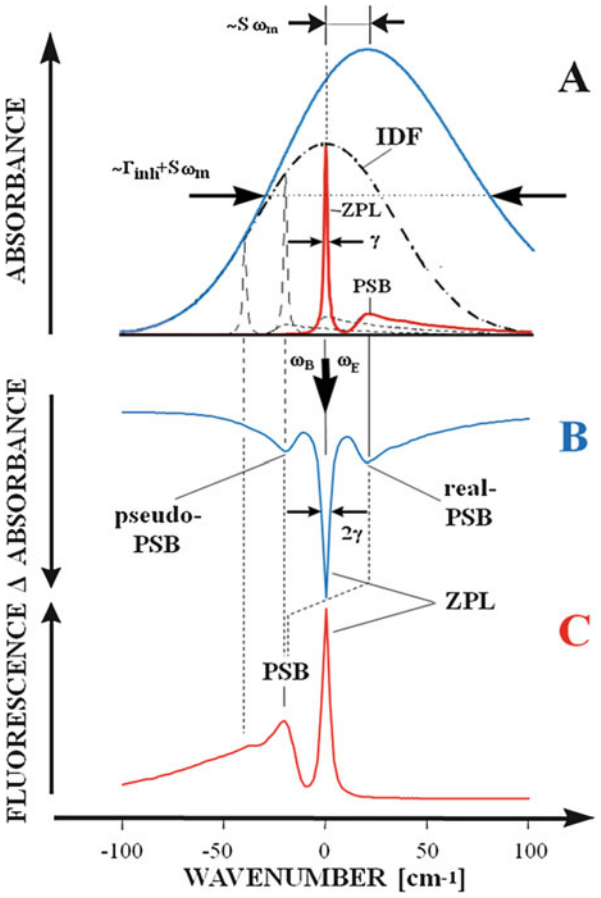


Fig. 2.3 Schematic illustration of conventional (Frame **A**) and line-narrowing spectroscopies (Frames **B** and **C**). Frame **A**: The homogeneously broadened absorption spectrum of a model pigment–protein complex shown as a *red line* consists of ZPL and an asymmetric PSB towards higher energies at low temperature. The homogeneously broadened spectrum is directly accessible only by SMS and delta-FLN spectroscopies, see text. In conventional absorption spectroscopy, however, inhomogeneous broadening has to be considered so that the resulting ensemble spectrum (*blue line*) is the convolution of the homogeneously broadened absorption spectrum with a Gaussian IDF (see *dashed dotted line*). The calculations were performed assuming an inhomogeneous width of 80 cm^{-1}, a Huang–Rhys factor of 1.0, and a phonon profile with a peak at 20 cm^{-1} and a width of $\Gamma = 20\ cm^{-1}$ ($\Gamma_G = 10\ cm^{-1}$, $\Gamma_L = 30\ cm^{-1}$). Frame **B** shows a SHB spectrum of the model pigment–protein complex introduced in Frame **A** (*blue line*). It consists of ZPL (or ZPH) and real-PSB towards the high-energy side of the ZPL. The latter features correspond to the homogeneously broadened absorption spectrum and appear due to resonant burning of pigment molecules, whose ZPL are resonant with the burn frequency ω_B (indicated by the *red spectrum* in Frame **A**). The additional pseudo-PSB lying towards the low-energy side of the ZPL is the result of nonresonant burning of pigment molecules whose PSB are resonant with the burn frequency ω_B (indicated by the *dashed spectra* in Frame **A**). Correspondences between features shown in Frames **A** and **B** are indicated by *full* and *dashed lines* for the cases of resonant and nonresonant burning, respectively. Frame **C** shows a FLN spectrum of the model pigment–protein complex introduced in Frame **A** (*red line*) consisting of ZPL and only a single PSB towards the low-energy side of the ZPL, because both, real-and pseudo-PSB, are found at the same side of the ZPL in the case of FLN. Adapted from [82]. Copyright 2000 J. Pieper

$$L(\omega) = e^{-s} l_0(\omega - \Omega) + \sum_{R=1}^{\infty} S^R \frac{e^{-S}}{R!} \; l_R(\omega - \Omega \mp R\omega_m). \tag{2.2}$$

In Eq. (2.2), the − and + signs correspond to absorption and fluorescence, respectively. The first term describes the ZPL with a Lorentzian shape l_0 at a frequency position Ω. The phonon sideband consists of all one-phonon and multi-phonon transitions forming the l_R-terms with ($R \geq 1$). Here, the terms for $R = 1$, $R = 2$, $R = 3$, ... correspond to one-quantum, two-quantum, three-quantum, ... and further multi-quantum transitions, respectively. This means that in case of a one-quantum transition peaking at ω_m, the two-quantum transition is found at $2\omega_m$, the three-quantum transition at $3\omega_m$, and any multi-quantum transition at $R\omega_m$. In order to account for the frequency dependence of absorption and fluorescence, Eq. (2.2) would have to be multiplied by ω and ω^3, respectively [11]. However, this effect is relatively small in the case of electron–phonon coupling given the relatively low phonon frequencies.

The one-quantum lineshape l_1 has a special meaning and is referred to as the spectral density, generally representing the distribution of all (delocalized protein as well as localized chromophore) vibrational modes, and their coupling strength to the electronic transition. Referring to electron–phonon coupling only, the shape l_1 is also denoted as the one-phonon profile. Comparing the protein and the chromophore vibrations, the 3N-6 chromophore frequencies collectively lie at higher energies than the delocalized protein vibrations, because of the smaller effective mass of the moving entities. Therefore, the chromophore vibrations are observed as individual narrow lines at higher energies than the phonon sideband.

The dynamics of energy transfer and relaxation processes is mostly determined by the quasi-continuum phonon part of the spectral density. Therefore, the total coupling strength of phonons to an electronic transition, governing the intensity distribution between the ZPL and the PSB, has a special interest [28]. It is characterized by a single dimensionless number, the Huang–Rhys factor S. The Huang–Rhys factor is associated with the displacement of the equilibrium positions of the nuclei upon a photoexcitation of the chromophore as illustrated in Fig. 2.2. Therefore, S is a measure for the strength of the linear electron–phonon coupling and characterizes the average number of phonons accompanying a particular electronic transition. It follows from Eq. (2.2) that the intensity share of ZPL (I_{ZPL}) yields the value of exp(−S), being equivalent to

$$\exp(-S) = \alpha = I_{ZPL}/(I_{ZPL} + I_{PSB}). \tag{2.3}$$

In addition, the strength of electron–phonon coupling is often expressed in terms of the Debye–Waller factor α that is also defined in Eq. (2.3). Typically, one distinguishes weak electron–phonon coupling with S-factors smaller than 1 and strong coupling with S-factors larger than 1. Although the Huang–Rhys factor has a rigorous meaning only within the Franck–Condon interaction model, it is widely used in a much broader context, even in case of excitons, as a general indicator of

Table 2.1 Huang–Rhys factor S obtained by SHB, FLN, and delta-FLN for the lowest energy states of different photosynthetic pigment–protein complexes[a]

Complex	S-factor	Method	Reference
Chl*a* in 1-propanol	0.56	Delta-FLN[b]	[60]
BChl*a* in triethylamine	0.46	Delta-FLN[b]	[61]
FMO from green sulphur bacteria	0.46	Delta-FLN[b]	[52]
LH1 from Rb. sphaeroides	1.6	Delta-FLN[b]	[73]
B850 band of LH2 from Rb. sphaeroides	2.0	Delta-FLN[b]	[73]
B800 band of LH2 from Rb. sphaeroides	0.1–0.9	SMS	[46]
CP43	0.30	SHB	[83]
			[84]
CP47	0.7	SHB	[85]
	1.0	SHB	[86]
CP29	0.50–0.68	Delta-FLN[b]	[54]
LHC I	2.9	FLN	[87]
LHC II monomer	0.62	Delta-FLN[b]	[69]
LHC II trimer	0.9	SHB/FLN	[50]
Chl*a* dimers In WSCP	0.81	Delta-FLN	[12]
Chl*b* dimers In WSCP	0.88	Delta-FLN	[12]
PS I core from cyanobacteria	2.0	SHB	[88]
P680 from PS II RC	1.9	SHB	[89]

[a]Obtained at the excitation/burn frequency corresponding to the half height of the IDF from the long-wavelength side
[b]Corrected values, see text

the exciton–phonon coupling strength. This operational approach based on Eq. (2.3) is also followed in the present text. An overview of the experimentally determined S-factors in case of isolated (B)Chls and several photosynthetic complexes, obtained by different line-narrowing techniques, is given in Table 2.1. The characteristic vibrational frequencies and corresponding coupling constants S for Chl*a* and Chl*b* are summarized in Table 2.2.

The phonon part of the one-quantum profile l_1 is within the mean frequency approximation represented by a product of the phonon density of states g(ω) and of a frequency-dependent electron–phonon coupling term s(ω). The one-phonon profiles determined for various photosynthetic complexes are typically broad and asymmetric lineshapes with a major peak at about 20–30 cm^{-1}. The shape l_1 can often be well approximated by a Gaussian at its low-energy side according to

$$l_R = \frac{2}{\Gamma_R \sqrt{\Pi/\ln 2}} \exp\left(- \left[\frac{\omega - \nu \mp R\omega_m}{\Gamma_R / 2\sqrt{\ln 2}} \right]^2 \right) \tag{2.4}$$

and a Lorentzian at its high-energy side according to

Table 2.2 Vibrational frequencies ν_j (± 2 cm^{-1}) and Huang–Rhys factors, S_j (± 0.0005) of Chl*a*-WSCP and Chl*b*-WSCP obtained by delta-FLN spectroscopy at 4.5 K [12]

Chl*a*-WSCP, ν_j (cm^{-1}) [12]	Chl*a*-WSCP, S_j [12]	CP29, ν_j (cm^{-1}) [54]	Chl*b*-WSCP, ν_j (cm^{-1}) [12]	Chl*b*-WSCP, S_j [12]	Chl*b*, ν_j (cm^{-1}) [58]
183	0.0078	192	181	0.0173	
228	0.0082		221	0.0246	
			240	0.0182	245
259	0.0160	262	269	0.0064	255
283	0.0052	287	283	0.0036	
			298	0.0104	310
327	0.0055		325	0.0112	
356	0.0245	350	352	0.0249	345
384	0.0147	386	366	0.0112	375
402	0.0088	401	405	0.0061	405
435	0.0085	425	430	0.0050	
			470	0.0075	465
481	0.0137	467	488	0.0061	
520	0.0157	517	515	0.0045	515
547	0.0042	545	537	0.0157	
574	0.0072	573	572	0.0132	560
584	0.0049		598	0.0036	595
609	0.0075	607	620	0.0047	625
656	0.0013		641	0.0033	
690	0.0013	701	700	0.0019	680
703	0.0019				700
718	0.0039		713	0.0025	
			734	0.0107	732
742	0.0353	745	746	0.0112	742
754	0.0212		757	0.0229	750
803	0.0101	800	800	0.0022	
816	0.0066				
840	0.0072	842	834	0.0140	832
			863	0.0033	
			887	0.0019	885
920	0.0251	918	922	0.0291	923
985	0.0158	989	977	0.0110	980
993	0.0129		998	0.0036	1,003
1,024	0.0068		1,023	0.0022	
1,047	0.0215	1,049	1,045	0.0056	1,040
1,067	0.0170	1,070	1,068	0.0050	1,070
1,104	0.0176	1,109	1,108	0.0087	1,087
			1,128	0.0011	1,120
1,144	0.0303	1,145	1,150	0.0244	1,140
1,184	0.0460	1,186	1,172	0.0121	
		1,227	1,186	0.0226	1,190
1,217	0.0502		1,227	0.0249	1,217
1,243	0.0176		1,243	0.0090	1,253
1,259	0.0101	1,262	1,264	0.0126	1,275

(continued)

Table 2.2 (continued)

Chl*a*-WSCP, ν_j (cm^{-1}) [12]	Chl*a*-WSCP, S_j [12]	CP29, ν_j (cm^{-1}) [54]	Chl*b*-WSCP, ν_j (cm^{-1}) [12]	Chl*b*-WSCP, S_j [12]	Chl*b*, ν_j (cm^{-1}) [58]
1,285	0.0193	1,286	1,288	0.0224	
1,304	0.0107	1,307	1,305	0.0093	
1,329	0.0389	1,329	1,326	0.0509	1,330
1,354	0.0105	1,353	1,360	0.0093	1,270
1,375	0.0094	1,374			
1,390	0.0173	1,387	1,393	0.0328	1,390
1,441	0.0232	1,439	1,443	0.0121	
1,490	0.0088	1,490	1,484	0.0107	1,480
1,532	0.0330	1,537	1,522	0.0185	1,515
1,556	0.0212	1,556	1,550	0.0241	1,540
1,591	0.0058		1,573	0.0182	
1,620	0.0091	1,610	1,628	0.0081	
1,649	0.0114	1,665	1,654	0.0135	
			1,681	0.0067	
Sum	0.80		Sum	0.74	

The vibrational frequencies are compared to those determined for Chl*a* in CP29 of green plants [54] and isolated Chl*b* in solution [58]

$$l_R = \frac{\Gamma_R/_{2\Pi}}{\left[\omega - \nu \mp R\omega_m\right]^2 + \left[\Gamma_R/_2\right]^2}, \tag{2.5}$$

where the width Γ_R is defined as $\Gamma^R_{gauß} = \sqrt{R}\Gamma^0_{gauß}$ and $\Gamma^R_{lorentz} = R\Gamma^0_{lorentz}$ in the case of a Gaussian and Lorentzian, respectively [27].

The two terms g(ω) and s(ω) cannot be determined individually by optical line-narrowing techniques; however, the density of phonon states, which represents the 3N-6 eigenfrequencies of the protein matrix, can be directly obtained using inelastic neutron scattering [29]. Based on neutron studies, the density of phonon states appears to be rather similar for many different proteins with broad and asymmetric lineshapes peaking at about 20–30 cm^{-1} [30–32]. However, its spectral form was shown to vary with protein size (see, e.g., [30]) and due to interaction with the solvent (see, e.g., [32]). More recent, temperature-dependent inelastic neutron scattering experiments indicated that the shape of the one-phonon profile may change with temperature increase and shift towards lower frequencies above the dynamical transition of the protein matrix at about 240 K [33]. The shape of the one-phonon profile can in principle be predicted by normal mode analysis and molecular dynamics simulations based on the crystal structure of a given protein [29, 32] and has recently been reported for the Fenna–Matthews–Olson complex [34]. Individual one-phonon profiles for several photosynthetic pigment–protein complexes are listed in Table 2.3.

Similar concepts as for isolated chromophores are applicable to exciton–phonon coupling in the photosynthetic complexes that bind the excitonically coupled

Table 2.3 One-phonon profiles l_1 obtained for the lowest energy states of different photosynthetic pigment–protein complexes assuming a Gaussian and Lorentzian lineshape at the low- and high-energy side of the mean phonon frequency ω_m

Complex	Mean phonon frequency, ω_m (cm^{-1})	FWHM of the Gaussian wing of the one-phonon profile l_1 (cm^{-1})	FWHM of the Lorentzian wing of the one-phonon profile l_1 (cm^{-1})	Reference
FMO from green sulphur bacteria	21	21	56	[52]
LH1 from Rb. sphaeroides	26	26	130	[73]
B850 band of LH2 from Rb. sphaeroides	28	28	80	[73]
CP29	22	20	130	[54]
LHC II trimer	18	16	160	[31]
Chl*a* dimers in WSCP[a]				[12]
Profile 1	24	25	25	
Profile 2	48	20	50	
Profile 3	88	24	60	

[a]A proper description of the highly structured PSB of WSCP delta-FLN spectra required the assumption of three individual one-phonon profiles, [12] for details

pigments with the following modifications. According to Davydov [13], within the adiabatic approximation, the exciton–bath interaction can be separated into two, diagonal and non-diagonal, parts. The diagonal part describes the modulation of the molecular (site) transition energies by spatial and orientational coordinates of the molecule and is primarily responsible for the phonon and vibrational/vibronic sidebands of the exciton spectra. Its physical origin is the change in dispersion interactions between the chromophores when one of the chromophores is electronically excited. The non-diagonal part of the interaction is due to variation of the inter-pigment (excitonic) coupling energies by nuclear motions. This term is mostly accountable for the phonon-assisted exciton relaxation. Assuming for simplicity only diagonal coupling (the dispersion force coupling limit [35]), a picture of mutually shifted excitonic potential energy surfaces arises, qualitatively similar to the one for individual chromophores shown in Fig. 2.3. However, due to delocalized nature of excitons as well as vibrations the Huang–Rhys factor (and the respective reorganization energy) corresponding to the specific exciton state is modified compared with that of individual chromophores. For equivalent diagonal coupling strength the electron–phonon coupling for an exciton state will be reduced relative to that for a localized excitation. This effect will be larger, the wider (the more spread) is the exciton band [35, 36]. Furthermore, since the extent of delocalization of different exciton states may be different, the reorganization energy and the Huang–Rhys factor may also vary from state to state [37]. The value of the Huang–Rhys factor for a selected exciton state can be accessed from the experimental phonon sideband using the same procedure (see Eq. 2.3) as in case

of localized excitations. Also similar criteria of weak ($S < 1$) and strong ($S > 1$) coupling apply. However, their physical meaning is different. In case of excitons the strength of the electron–phonon coupling involves a propagation aspect. At $S \ll 1$ excitons are free, almost not disturbed by lattice vibrations. In contrast, when $S \gg 1$ the exciton is completely localized (self-trapped) by the on-site or local electron–phonon coupling. Various situations in between can be described as excitons propagating in the form of an exciton polaron, i.e., of an electronic excitation, which is accompanied by lattice phonons [38]. The exciton polaron effects discovered in bacterial light-harvesting complexes will be briefly introduced in the last Section of this treatise. Vibrational sidebands of excitonic transitions in dye aggregates and biological light-harvesting complexes are presently a matter of active study. The physical insights and computational methodologies of this research area can be found in [10, 39–43].

2.3 Encounter with the Reality: Inhomogeneous Broadening

As already noted in Introduction, a direct experimental determination of single site spectra of photosynthetic pigment–protein complexes (illustrated by red line in Frame A of Fig. 2.3) can only be achieved by low-temperature SMS, which remains a challenging task, although a number of successful single-molecule studies have been reported since 1999 ([44–48]). On the other hand, conventional absorption and fluorescence spectra are widely structureless because of significant inhomogeneous broadening of optical transitions of the pigments embedded in amorphous protein matrices [5].

Generally speaking, broadening mechanisms are considered to be *homogeneous* when affecting an optical transition of all molecules in an ensemble in the same way. Therefore, single-molecule spectra are by definition homogeneously broadened spectra. Ensemble spectra may be *inhomogeneously* broadened, because the specific environment of a pigment embedded into an amorphous matrix (including proteins) may differ from protein to protein in a bulk sample, affecting the transition frequency of that molecule. Static inhomogeneous broadening of photosynthetic pigment–protein complexes is usually well approximated by a nearly Gaussian distribution with full widths Γ_{inh} in the order of 80–200 cm^{-1} [5], which is referred to as inhomogeneous distribution function (IDF). Here, Γ_{inh} can be viewed as a measure for the inherent heterogeneity of the protein matrix. Sometimes, the IDF is also called site distribution function (SDF); however, this notation might occasionally interfere with the term *pigment binding site* in photosynthetic complexes. Therefore, we stick with a unique IDF, which does not include contributions from different pigment sites, but denotes a distribution of transition frequencies for the pigments at one and the same binding site in a bulk sample due to different protein conformations.

Based on the above considerations, the absorption and fluorescence spectra for an ensemble of pigments in an amorphous protein host at low temperatures are obtained through a convolution of the homogeneously broadened spectrum of Eq. (2.2) with a Gaussian IDF denoted as N (Ω_0-ω_C)

$$L(\omega) = \sum_{R=0}^{\infty} \left(S^R \frac{e^{-S}}{R!} \right) \int d\Omega_0 N(\Omega_0 - \omega_C) l_R(\omega - \Omega_0 \mp R\omega_m). \tag{2.6}$$

In Eq. (2.6), the $-\mathrm{R}\omega_\mathrm{m}$ and $+\mathrm{R}\omega_\mathrm{m}$ terms correspond to absorption and fluorescence, respectively, and the IDF function N ($\Omega_0-\omega_C$) of full width of Γ_inh peaks at ω_C.

The mutual relationships between the homogeneously and inhomogeneously broadened spectra are illustrated by model simulations presented in Fig. 2.3, Panel A. Due to the main focus of this chapter on electron–phonon coupling, these and the subsequent simulations include only phonon modes. The homogeneously broadened absorption spectrum (bold red line) is calculated according to Eq. (2.2). The intensities of the ZPL are distributed according to a Gaussian IDF with $\Gamma_\mathrm{inh} = 80\ \mathrm{cm}^{-1}$ (dashed-dotted line). The resulting inhomogeneously broadened absorption spectrum is calculated according to Eq. (2.6) (bold blue line). As known from the experiments performed under non-line-narrowing conditions, the latter spectrum appears to be widely structureless. When $\omega_\mathrm{m} < \Gamma_\mathrm{inh}$, the separate ZPL and PSB features are wholly masked by the relatively broad IDF, which determines the spectral resolution of conventional spectroscopy. The only apparent signature of the electron–phonon coupling is a slight asymmetry of the inhomogeneously broadened spectrum towards higher energies as well as a shift between the purely electronic transition at the center of the IDF and the absorption maximum, denoted as $\mathrm{S}\omega_\mathrm{m}$. Assuming mirror symmetry between the absorption and fluorescence spectra around the ZPL, the shift between the absorption and fluorescence maxima, referred to as *Stokes shift*, can in the mean phonon frequency approximation be estimated to be equal to twice the reorganization energy [27]

$$\Delta\omega_\mathrm{Stokes} \sim 2\ \mathrm{S}\omega_\mathrm{m}. \tag{2.7}$$

On the same footing, the width of the non-line-narrowed absorption spectrum is approximately [27]

$$\Gamma_\mathrm{non\text{-}line} \sim \Gamma_\mathrm{inh} + \mathrm{S}\omega_\mathrm{m}. \tag{2.8}$$

Equations (2.7) and (2.8) hold the better the narrower is the one-phonon profile, i.e., the better validated is the mean phonon approximation.

In summary, it is apparent from the simulations presented in Fig. 2.3 that any phonon structure is hidden by inhomogeneous broadening in conventional spectra, so that spectrally selective experimental techniques are necessary to unravel information on electron–phonon coupling in photosynthetic pigment–protein complexes. The static fluctuations of the environment, believed to be the main cause of

inhomogeneous broadening of optical spectra, can formally be looked at as a kind of a random noise that modulates the molecular transition energies, i.e., spectral positions of ZPL. Possible modifications of the homogeneous shapes of the spectra, which are related to electron–phonon and/or vibronic couplings, are ignored by this approach. As will be shown in the final part of the chapter, this view turns out to be too simplistic. In reality the total electron–phonon coupling strength depends on the excitation frequency both for localized excitations and for excitons.

2.4 Phonon Structure in Selectively Excited Spectra

In general, all line-narrowing techniques (SHB, FLN, delta-FLN) are based on selective laser excitation within an inhomogeneously broadened absorption profile at low temperatures, which selects information from only a subset of pigment molecules absorbing at a certain burn/excitation frequency. In SHB experiments, the transition frequency of those molecules/states selected by the burn laser is altered, so that the difference between pre- and post-burn absorption spectra reveals a hole at the burn frequency and a concomitant increase of absorption at another frequency. The latter gain in absorption is referred to as anti-hole or photoproduct depending on the mechanism of hole burning. For details on the different SHB mechanisms see Jankowiak et al. [5] and references therein.

A SHB spectrum for a model pigment–protein complex is shown in Frame B of Fig. 2.3. This spectrum exhibits a sharp zero-phonon hole (ZPH) at the burn frequency ω_B and different PSB holes on the low- and high-energy sides of the ZPH, respectively. Comparison with the single site absorption spectrum in Frame A of Fig. 2.3 shows that the ZPH is due to resonantly burned electronic transitions overlapping the burn frequency ω_B. The width of the ZPH is twice the homogeneous linewidth γ, because the burn laser does not only select perfectly resonant ZPL, but also those absorbing via their Lorentzian wings. Here, it is assumed that the laser linewidth is much narrower than the ZPL width γ. The feature at the high-energy side of the ZPH is the real-PSB, which is due to the phonon sidebands of the resonantly burned ZPH. Therefore, ZPH and real-PSB correspond directly to ZPL and PSB of the homogeneously broadened absorption spectrum, respectively, shown by the bold red line in Frame A of Fig. 2.3. In addition, there are electronic transitions within the IDF, which are nonresonantly overlapping the burn frequency ω_B via their phonon sidebands (see dashed lines in Frame A of Fig. 2.3). Following fast relaxation into the zero-phonon energy levels, the burn process becomes effective at the ZPL positions of those nonresonantly selected pigment molecules. As a result, these transitions form an additional feature named pseudo-PSB, which in ideal case forms the mirror image of the real-PSB. Electronic transitions at higher energy than ω_B do not contribute to the hole-burned spectrum. The corresponding FLN spectrum is shown in Frame C of Fig. 2.3. The latter spectrum exhibits a ZPL and only a single PSB feature. The reason for this observation is that the real-PSB

lies on the low-energy side of the ZPL in fluorescence and is, therefore, superimposed on the pseudo-PSB.

In a next step, expressions for the line-narrowed spectra of a pigment–protein system shall be developed. As for SHB, the pre-burn (absorption) spectrum A ($\tau = 0$, ω) at the burn time $\tau = 0$ is given by Eq. (2.6) [27]. SHB produces a persistent loss of absorption for a distinct electronic transition selected by the burn laser frequency. Upon exposure to the burn frequency ω_B during time τ the IDF is modified as given by [27]

$$N(\tau, \Omega_0 - \omega_C) = N(\Omega_0 - \omega_C)\exp[-\sigma I \Phi \tau L(\omega_B - \Omega_0)], \tag{2.9}$$

where the exponential term describes the hole growth due to the burn process. The lineshape $L(\omega_B\text{-}\Omega_0)$ corresponds to the homogeneously broadened absorption spectrum as given by Eq. (2.2). ZPL and PSB of this lineshape represent those electronic transitions within the IDF that are bleached resonantly and nonresonantly, respectively. Each of the purely electronic transitions burned according to Eq. (2.9) carries a finite width γ of the ZPL and is accompanied by a PSB. Therefore, the homogeneously broadened absorption spectrum (Eq. 2.2) has to be convoluted with the modified IDF (Eq. 2.9) to yield the entire absorption spectrum after a burn time τ, which is given by [27]

$$\begin{aligned} A(\tau, \omega) = \sum_{R=0}^{\infty} \left(S^R \frac{e^{-S}}{R!} \right) \int d\Omega_0 N(\Omega_0 - \omega_C) \times \\ \exp[-\sigma I \Phi \tau L(\omega - \Omega_0)] l_R(\omega - \Omega_0 - R\omega_m). \end{aligned} \tag{2.10}$$

The total SHB spectrum is then obtained as the difference between the absorption spectrum at the burn frequency ω_B at the burn time τ and the pre-burn absorption spectrum at the start of the experiment, i.e.,

$$\Delta A(\omega) = A(\tau, \omega) - A(\tau = 0, \omega) \tag{2.11}$$

In order to be concise, we will not discuss effects of arbitrary burn fluence in the present chapter. Rather, the reader is referred to comprehensive reviews for further information (e.g., Jankowiak et al. [5]). In the low-fluence limit expanding the exponential in Eq. (2.10) into a Taylor series and neglecting second and higher order terms one obtains the SHB spectrum:

$$\begin{aligned} \Delta A(\omega) = \sum_{R,P=0}^{\infty} \left(S^R \frac{e^{-S}}{R!} \right) \left(S^P \frac{e^{-S}}{P!} \right) \int d\Omega_0 N(\Omega_0 - \omega_C) \times \\ l_P(\omega_B - \Omega_0 - P\omega_m) l_R(\omega - \Omega_0 - R\omega_m), \end{aligned} \tag{2.12}$$

where l_P represents the electronic transitions bleached during the burn process. For simplicity, the pre-factor $\sigma P \phi \tau$ was set to unity here. In the low-fluence limit, this

has no effect on the shape of the spectrum. The FLN spectrum can be expressed in a rather similar form, if the term $-R\omega_m$ in the homogeneously broadened lineshape l_R is replaced by $+R\omega_m$ to account for fluorescence.

All the above considerations as well as the model calculations presented in Fig. 2.3 assume that real- and pseudo-PSB are mirror symmetric, which is valid only in cases where the inhomogeneous width is much larger than the width of the one-phonon profile Γ, i.e., $\Gamma_{inh} \gg \Gamma$. In this regard it is important to note that SHB and FLN results obtained for the antenna complex LHC II of green plants [49, 50] have established a width of the phonon sideband of ~ 100 cm^{-1} comparable or even broader than the inhomogeneous width of only ~80 cm^{-1}. Therefore, following [51], we will now consider the different PSB contributions in the $\Gamma_{inh} \approx \Gamma$ regime. The simulated FLN and SHB spectra are shown by dashed curves in Frame A and Frame B of Fig. 2.4, respectively. Specific parameters of these calculations are provided in the figure caption. It is obvious from Fig. 2.4 that the real- (contribution b) and pseudo-PSB (contribution c) exhibit clearly different shapes in both SHB and FLN spectra. The PSB of the dashed FLN spectrum and the real-PSB of the dashed SHB spectrum show features at 15 and 26 cm^{-1} that correspond to one- and two-quantum transitions of phonons with $\omega_m = 15$ cm^{-1}. The two-quantum transition and the slight tailing towards higher phonon frequencies, however, are not observed in the pseudo-PSB of the dashed spectrum in Frame B, i.e., the mirror symmetry between real- and pseudo-PSB breaks down in the $\Gamma \approx \Gamma_{inh}$ regime. This is because the pseudo-PSB is governed by the quickly tailing Gaussian IDF rather than by the slowly tailing Lorentzian wing of the one-phonon profile. The latter point is nicely illustrated in frame A of Fig. 2.4 where it is obvious that the IDF determines the shape of the pseudo-PSB (c) on its low-energy side. These findings suggest that accurate extraction of Huang–Rhys factors from SHB spectra requires a careful analysis, especially for systems in which the width of the PSB is similar to or larger than that of the IDF. Although SHB in principle provides real- and pseudo-PSBs as separate features (see above), the real-PSB is often interfered with by the anti-hole, so that the one-phonon profile is routinely obtained from the more intense pseudo-PSB.

In the limit of an infinitely wide IDF and low-fluence, this approximation would be perfectly justified since the real- and pseudo-PSB terms, being mirror symmetric, provide exactly the same information. Based on the argumentation above, however, it can be expected that in real systems, the one-phonon profile determined this way will not reflect the correct tailing at its high-energy side, particularly for systems in which the IDF is narrow relative to the PSB. As a result, Huang–Rhys factors calculated from the areas of ZPL and pseudo-PSB would generally be artificially lowered, with the extent of lowering depending on the burn wavelength and the relative widths of the IDF and PSB.

More recently, a new method for obtaining electron–phonon coupling parameters called delta-FLN spectroscopy [52] emerged, which is capable of overcoming the shortcomings of SHB and FLN spectroscopy discussed above. Earlier realizations of this technique [19, 20] have been applied to enhance spectral selectivity of FLN mainly in the range of vibronic lines. The approach of Rätsep and Freiberg,

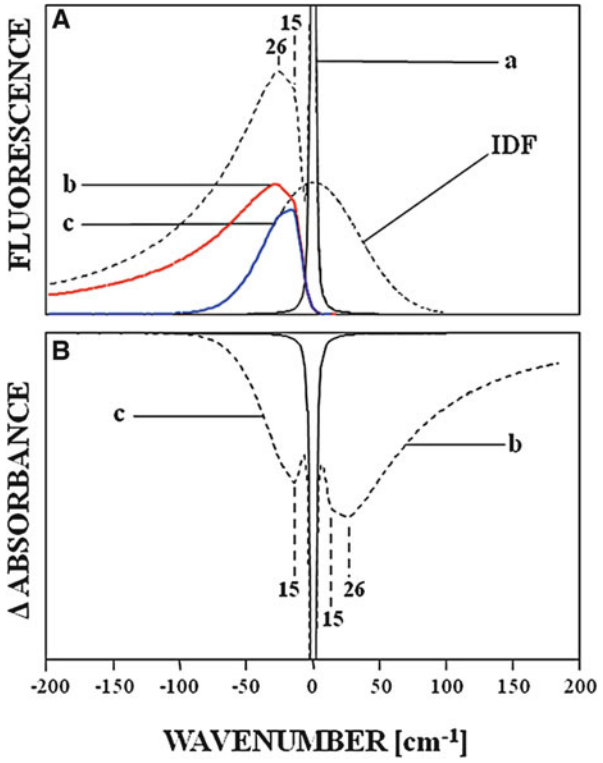


Fig. 2.4 Low-temperature line-narrowed fluorescence (Frame **A**) and hole-burned (Frame **B**) spectra (*dashed lines*) simulated according to Eq. (2.12), respectively, for illustration of the $\Gamma_{inh} \sim \Gamma$ regime. The calculations were performed assuming an inhomogeneous width of 80 cm^{-1}, a Huang–Rhys factor of 1.0, and a phonon profile with a peak at 15 cm^{-1} and a width of $\Gamma = 57.5$ cm^{-1} ($\Gamma_G = 15$ cm^{-1}, $\Gamma_L = 100$ cm^{-1}), i.e., in contrast to the simulations shown in Fig. 2.3, the Lorentzian tailing of the one-phonon profile does exceed Γ_{inh}. In Frame **A**, the *full black line* represents the ZPH (a), the *red line* is the real-PSB (b), and the *blue line* is the pseudo-PSB (c). In Frame **B**, the real-PSB and the pseudo-PSB contributions are labelled by b and c, respectively. The multi-PSBs are omitted for clarity and the zero-phonon lines are cut off at 4 % of their peak intensity value. The *dashed-dotted line* represents the profile of the IDF. Note the breakdown of mirror symmetry between the real-PSB and the pseudo-PSB contributions visible in both frames and the high-energy tailing of the pseudo-PSB determined by the shape of the IDF. Reprinted with permission from Pieper et al. [51]. Copyright 1999 Elsevier B.V.

however, readily yields the ZPL together with the phonon and vibrational structure building on it so that electron–phonon and electron–vibrational coupling strengths can be uniquely determined.

A delta-FLN spectrum is obtained as the difference between FLN spectra recorded before and after an intermediate hole-burning step. This technique provides two important advantages over traditional SHB and FLN spectroscopy: first, the scattered laser light which otherwise obscures the ZPL in FLN spectra can be

effectively eliminated in the difference spectrum, allowing direct measurement of the ZPL; second, the "double selection" via both SHB and FLN suppresses the pseudo-PSB term in the low-fluence limit, so that the final delta-FLN spectrum becomes identical to the homogeneously broadened spectrum [19, 20, 53].

Theoretically, the delta-FLN spectrum is obtained by subtracting pre- and post-burn FLN spectra according to delta-FLN(ω) = FLN(τ,ω) − FLN(τ = 0, ω). Here, the pre-burn spectrum FLN(τ = 0, ω) is identical to Eq. (2.12), while the post-burn FLN spectrum FLN(τ,ω) is best derived from Eq. (2.6) by replacing the IDF term by N (Ω_0-ω_C) modified by the burn process. Accordingly, the post-burn FLN spectrum can be written as

$$\Delta FLN(\tau,\omega) = \sum_{R,P=0}^{\infty} S^R \frac{e^{-S}}{R!} S^P \frac{e^{-S}}{P!} \int N(\Omega_0 - \omega_C) \times \exp[-\sigma I \Phi \tau L(\omega - \Omega_0)] \times l_R(\omega_E - \Omega_0 - R\omega_m)\, l_P(\omega - \Omega_0 \mp P\omega_m)\, d\Omega_0 \tag{2.13}$$

Note in this regard that Eq. (2.13) contains two absorption lineshapes: first, L due to the hole-burning process, and second, l_R due to the selective excitation of the post-burn FLN spectrum. This difference leads to the "double selection effect" in delta-FLN [19, 20, 53], which is more apparent when Eq. (2.13) is specified for the low-fluence limit:

$$\Delta FLN(\omega) = k\, e^{-3S} \sum_{R,P=0}^{\infty} \frac{S^Q}{Q!} \frac{S^R}{R!} \frac{S^P}{P!} \int d\Omega_0 N(\Omega_0 - \omega_C) \times l_Q(\omega_E - \Omega_0 - Q\omega_m)\, l_R(\omega_B - \Omega_0 - R\omega_m)\, l_P(\omega - \Omega_0 + P\omega_m) \tag{2.14}$$

Except for writing down all terms explicitly, this equation is identical to that of Reppert et al. [53]. To discuss the difference between delta-FLN on one hand and FLN/SHB on the other in the low-fluence limit, this equation has to be compared to Eq. (2.12). It emerges that Eq. (2.14) contains the absorption lineshape describing the selective excitation twice as l_R and l_Q (identical to the quadratic term in [53]), while this term appears only once in the comparable expression for FLN (Eq. 2.12). Since the ZPL and PSB of the latter term represent resonant and nonresonant excitation, respectively, the multiplication of l_R with l_Q leads to an enlargement of the ZPL and a suppression of the PSB in the expression for delta-FLN and thus to a suppression of the nonresonantly excited pseudo-PSB. Some of the earlier delta-FLN results have, unfortunately, been analyzed in terms of Eq. (2.12) so that the S-factors obtained were somewhat underestimated by a maximum of 20 % in the case of CP29 [54]. Table 2.1 contains the corrected values of S assuming that the delta-FLN spectrum in the low-fluence limit reflects the homogeneously broadened fluorescence spectrum.

2.5 Results for Selected Photosynthetic Systems

Chlorophylls are ubiquitous photosynthetic chromophores in plants and algae, similar to BChls in bacterial systems [55]. The useful functioning of these molecules is based on their unique quantum-optical and redox properties. Being the lowest-energy electronic transitions in the visible range, the Q_y singlet electronic transitions are instrumental in all photophysical and photochemical processes these pigments are involved in. Their properties in dependence on solvent polarity, axial coordination of the central magnesium atom, pigment aggregation, temperature, pressure, electric and magnetic field, etc. have experimentally been studied using almost all conceivable spectroscopic techniques. Despite this intensive scrutiny, optical spectroscopy of the (B)Chl molecules is still not fully understood, neither experimentally nor theoretically [42, 56, 57]. Avarmaa and co-workers [58] were the first to obtain high-resolution spectra related to the Q_y electronic state of the impurity Chl*a* and BChl*a* molecules. Yet these low-temperature results had rather qualitative than quantitative value, since experimental limitations prohibited determination of the coupling strengths for both the bath phonons and individual intramolecular vibrations. As follows we will discuss a few basic experimental results, achieved by the delta-FLN method on the (B)Chl*a* pigment molecules either in isolation or when bound by the major photosynthetic light-harvesting complexes of green plants (LHC II) and purple bacteria (LH2).

*2.5.1 Isolated Photosynthetic Chromophores: Chl**a** and BChl**a***

Mirror symmetry between the conjugate absorption and emission spectra is theoretically expected within the model framework of the crude adiabatic, Condon, and harmonic approximations, assuming linear electron–phonon and vibronic coupling (this set of approximations is known as the basic model [11]), together with postulation of a fast excited state relaxation (the Kasha–Vavilov rule [59]). Whether or not asymmetry exists between the (B)Chl Q_y absorption and emission spectra has for a long time been an unsettled question. The experimental data concerning this problem were not only scarce but also controversial. While quantitative quantum chemical modeling of the absorption and emission spectra should in principle reveal the nature of the electronic transitions and the origin of any spectral asymmetry, without proper experimental guiding this is a challenging task for the chlorophyll type molecules owing to their relatively large size and extended conjugation.

The deviations from mirror symmetry in optical absorption and fluorescence emission spectra of Chl*a* and BChl*a* molecules were experimentally studied in [60, 61] using different solvents to induce either penta- or hexa-coordination of the central Mg atom. Based on the data obtained at different temperatures, one can

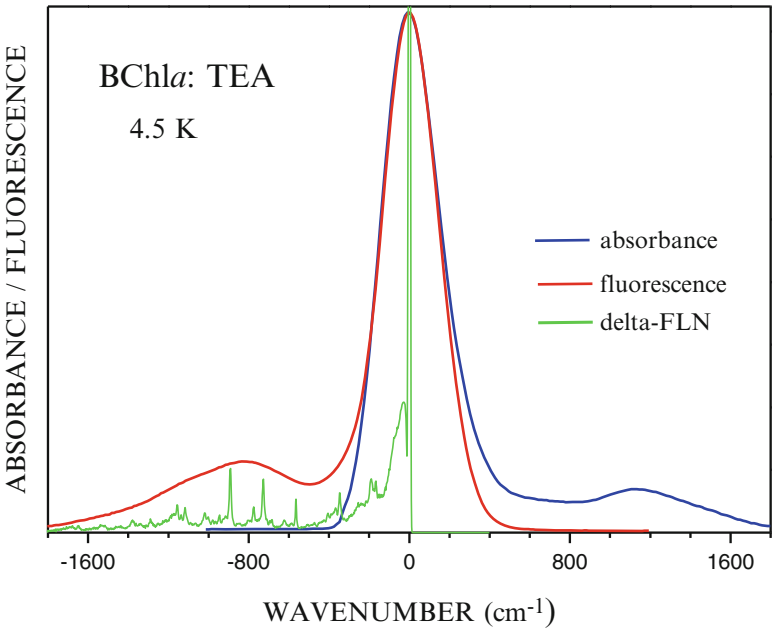


Fig. 2.5 Comparison of the frequency-weighted absorption (intensity/ω, *blue*) and (intensity/ω^3, *red*) spectra of BChl*a* in triethylamine (TEA) recorded at 4.5 K. The fluorescence was nonselectively excited at 405 nm. Revealed from the inhomogeneously bradened fluorescence lineshape is the homogeneously broadened delta-FLN spectrum (*green*), which comprises a narrow ZPL at zero frequency together with its phonon and vibrational sidebands extending towards lower frequency. See text for further details

safely conclude that mirror symmetry does not hold at any temperature between 4.5 K and ambient temperature neither in Chl*a* nor in BChl*a* molecules. In the BChl*a* emission (see Fig. 2.5), for example, the low-resolution vibronic sideband structure is centered on modes at ~900 cm^{-1}, while in absorption this band moves out to 1,100–1,200 cm^{-1}. In environments with sixfold-coordinated Mg, the emission sideband is considerably stronger, resulting in the corresponding reorganization energy being slightly larger than the reorganization energy in absorption. In fivefold-coordinated environments, however, the absorption value is 50 % larger than the emission value. Most computational methods predict the spectral asymmetry to be very much larger than that actually observed [62]; only the long-range corrected density functional CAM-B3LYP reproduced detailed experimental results for BChl*a* and predicted asymmetry of the correct magnitude. These simulations also revealed that the spectral asymmetry arises primarily through Duschinsky rotation [61]. In the case of the Chl*a* molecule the deviation from the mirror symmetry between the conjugated absorption and fluorescence spectra was assigned to a combined effect of Franck–Condon and Herzberg–Teller interactions [60]. A detailed analysis of the breakdown of mirror symmetry between fluorescence and fluorescence excitation spectra of arylpolyene molecules dissolved in the

n-octane matrix in terms of Franck–Condon and Herzberg–Teller interactions can be found in [63]. In case of Chl*a*, however, the most recent analyses [64] exposed a fundamentally new mechanism for the spectral asymmetry, which may overshadow the above Franck–Condon and Herzberg–Teller mechanisms. This is the strong coupling between the energetically closely spaced Q_y and Q_x excited electronic states, mediated by high-frequency intramolecular vibrations.

2.5.2 LHC II Antenna Complex of Green Plants

LHC II is the major light harvesting complex of higher plants and green algae. Its importance is underlined by the fact that it accounts for approximately 65 % of the Chl of photosystem II. LHC II is believed to occur in trimeric form, where each monomeric subunit binds 8 Chl*a* and 6 Chl*b* molecules [65, 66]. Electron–phonon coupling of the lowest energy level of trimeric LHC II has been intensively studied by all the selective spectroscopy techniques described in this chapter: SHB [49, 67], FLN [50, 68], and delta-FLN [69]. Initially, however, the results derived from the different techniques appeared to be rather diverse. SHB results suggested weak electron–phonon coupling with $S = 0.8$ and a rather narrow one-phonon profile with a peak at ~18 cm^{-1} and a width of only ~25 cm^{-1} [49]. In contrast, FLN data yielded slightly higher mean phonon frequencies of 22–24 cm^{-1} and systematically wider and more asymmetric one-phonon profiles with a width of ~65 cm^{-1} [68]. In the latter study, the S factor could not be directly obtained, because the ZPL is typically hidden by intense scattered laser light in FLN spectra. The different shapes of the PSBs obtained by SHB and FLN, respectively, are directly visible in Fig. 2.6 (data taken from Pieper et al. [49] and Pieper et al. [50]).

In this regard it is important to recall that the width of the widely asymmetric phonon sideband revealed by FLN is of the same order of magnitude as the inhomogeneous width of ~80 cm^{-1}, determined by constant fluence SHB spectroscopy [49]. As demonstrated by the model calculations for the $\Gamma_{inh} \sim \Gamma$ regime above (see Fig. 2.4), a breakdown of the mirror symmetry between the real- and pseudo-PSB contributions can be expected in this case even in the limit of linear Franck–Condon coupling. Consequently, the SHB and FLN data shown in Fig. 2.6 can be simultaneously modeled assuming a Huang–Rhys factor of ~0.9 and one and the same broad and strongly asymmetric one-phonon profile peaking at ~15 cm^{-1}. In the case of SHB, however, analysis had been based on the pseudo-PSB, which is cut off by the narrow IDF found for the lowest Q_y-state of LHC II at ~680.0 nm. This is further illustrated in Fig. 2.6, where the pseudo-PSB contributions to SHB and FLN are plotted individually and labeled by full arrows in Frames A and B. It is apparent that the pseudo-PSB contribution simulated for FLN is similar to the one directly visible in SHB. In the case considered here, the advantage of FLN lies in the accessibility of the real-PSB, which is undisturbed by the narrow IDF. The same feature is hardly visible in SHB (see Frame B of Fig. 2.6), because as described above it is refilled by the anti-hole produced during the burn process. These results

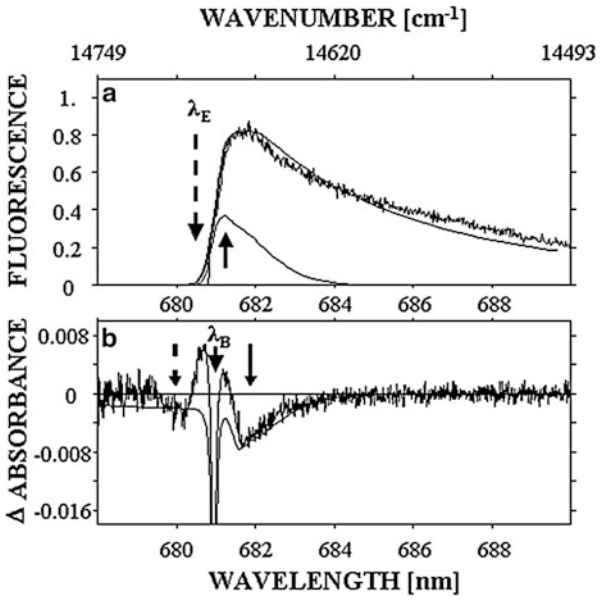


Fig. 2.6 Analysis of phonon structure in SHB and FLN spectra of trimeric LHC II at 4.2 K. Frame **a**: FLN spectrum (*noisy line*) experimentally obtained by selective laser excitation within the lowest energy state of LHC II with $\lambda_E = 680.5$ nm (see *dashed arrow*). The ZPL contaminated with scattered laser light has been subtracted for clarity. The fit of the FLN spectrum was calculated according to Eq. (2.13) (*smooth line*). The feature labeled by a *full arrow* is the simulated pseudo-PSB, whose shape differs significantly from the entire phonon sideband, but proves to be rather similar to pseudo-PSB observed directly by SHB in Frame **b**. Data are taken from Pieper et al. [51]. Frame **b**: Experimental SHB spectrum (*noisy line*) experimentally obtained with $\lambda_B = 681.0$ nm and a burn fluence of 15 J/cm^2. The real- and pseudo-PSB are indicated by *full* and *broken arrows*, respectively. The fit was calculated according to Eq. (2.12) with $\gamma = 0.2$ cm^{-1} and $\sigma I \Phi \tau = 0.003$ (*smooth line*). Reprinted with permission from Pieper et al. [51]. Copyright 1999 Elsevier B.V.

indicate that the apparent breakdown of mirror symmetry between real- and pseudo-PSB in the case of LHC II is a purely technical effect and not comparable to the spectral subtleties discussed in the previous paragraph for (B)Chl. In summary, a simultaneous modeling of SHB and FLN spectra of LHC II is necessary to obtain the correct parameters of electron–phonon coupling [21, 51].

The parameters of electron–phonon coupling of trimeric LHC II reviewed above have been further corroborated by delta-FLN spectroscopy [69]. In Fig. 2.7 a pre-burn FLN spectrum selectively excited within the fluorescence origin band of LHC II is shown as a black curve for a representative excitation wavelength of 682 nm. As expected, the spectrum is composed of a sharp ZPL located at the excitation wavelength and the broad phonon sideband peaking about 22 cm^{-1} to the red of the ZPL. In this spectrum the ZPL is still contaminated with scattered light originating from the excitation laser. An additional FLN spectrum (blue curve) was recorded after hole burning at the excitation wavelength with a burn fluence of 32 mJ/cm^2 shown as a blue curve in Fig. 2.8. The delta-FLN spectrum (red curve) is

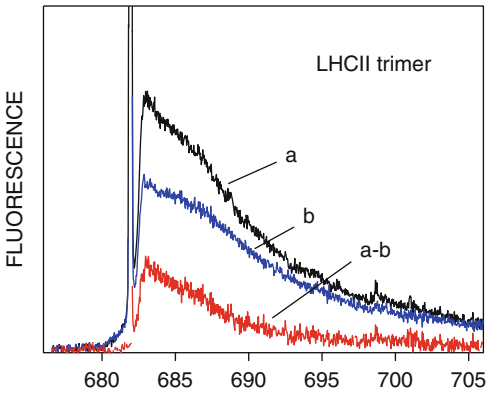


Fig. 2.7 Experimental 4.5 K delta-FLN spectra of trimeric LHC II excited/burned at 682.0 nm (*lower red curve*). The ZPL is cut off at 3.7 % of its full intensity for ease of inspection. The *black* (a) and *blue curves* (b) show the corresponding pre- and post-burn FLN spectra, respectively. FLN spectra were recorded with a fluence of 0.4 mJ/cm^2, while the fluence applied for hole burning was 32 mJ/cm^2. Reprinted with permission from Pieper et al. [69]. Copyright 2009 American Chemical Society

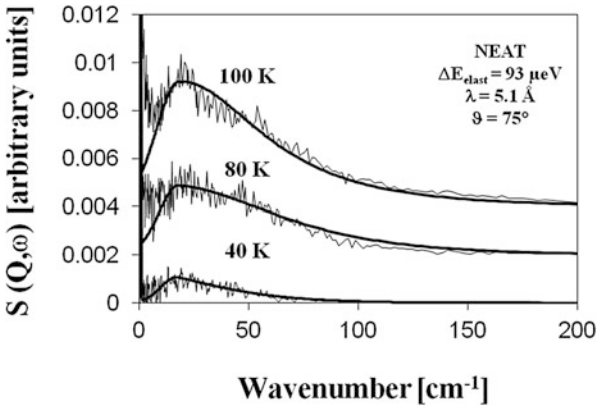


Fig. 2.8 Temperature dependence of INS spectra of trimeric LHC II obtained with an incident neutron wavelength of 5.1 Å and an elastic resolution of ~0.75 cm^{-1}. The spectra are given equidistant offsets of 0.002 for ease of inspection. The smooth, full lines correspond to theoretical fits (see text for details). Reprinted with permission from Pieper et al. [31]. Copyright 2004 American Chemical Society

readily obtained by subtracting the post-burn FLN spectrum from the pre-burn spectrum. The latter spectrum now consists of both the ZPL and PSB, because the subtraction procedure widely eliminates the scattering contribution and thus provides a reliable measure of the ZPL intensity. A Huang–Rhys factor S of 0.88 can be directly obtained from the delta-FLN spectrum, which turns out to be practically the same value reported above from the simultaneous fits of SHB and FLN spectra [51].

To the best of our knowledge, LHC II is the only isolated photosynthetic antenna complex that has been investigated by inelastic neutron scattering (INS) in order to directly obtain the phonon density of states [31]. Low-temperature INS spectra of LHC II are presented in Fig. 2.8. The data can be well described by a one-phonon function $S_1(\omega)$ with a maximum at 18.4 cm^{-1} as well as Gaussian and Lorentzian widths of 16 and 160 cm^{-1} at their low- and high-energy sides, respectively. Widely similar parameters were employed before to model the SHB and FLN results shown in Fig. 2.6 under the reasonable assumption that the electron–phonon coupling strength $s(\omega)$ is quite uniform in the investigated range of vibrational frequencies. This finding is a further proof for a rather broad and asymmetric distribution of phonon frequencies in LHC II as derived before from SHB and FLN.

2.5.3 *Strong Exciton–Phonon Coupling in the LH2 Antenna Complexes of Purple Bacteria*

The idealized exciton states in deformable (soft) lattices interact with the local vibrations of the molecular units themselves as well as with the collective phonons of the surroundings, leading (like in individual molecules albeit more complex ways) to dissipation of excitations as well as to vibronic and electron–phonon spectral structures, respectively. The same interactions, which increase with temperature, also govern decoherence and transport dynamics of excitons. To envision the latter effects, one could picture a moving exciton dragging behind a cloud of phonons, an exciton polaron. The thicker the cloud, the slower moves the exciton. In the limiting scenario the exciton may stop moving altogether localizing on a small region of the lattice. "This latter phenomenon is called exciton "self trapping" [38]."

A strong ($S > 2$) exciton–phonon coupling has been found [70–73] in fluorescence spectra of the ring-shaped B850 aggregates of BChl*a*, which is a part of the LH2 bacterial antenna complex, several times greater than observed for the monomeric BChl*a* chromophores in similar protein environments [52]. This is unexpected, since coupling in case of excitons should be several times smaller than in case of respective localized excitations due to "motional reduction" [38]. A visible consequence of such a strong exciton–phonon interaction is a broad multi-phonon PSB.

The Frenkel exciton model [1] as well as its various modifications such as the Redfield theory, which assume negligible exciton–lattice interactions, cannot capture strong coupling effects. A theoretical model involving dynamic exciton polaron formation in the spirit of Holstein [74], Heeger [75], and others has, therefore, been developed by us to explain the conflicting observations in case of the LH2 complexes [71, 73, 76, 77]. The fundamental nature of this model is that due to strong exciton–phonon interaction a structural reorganization of the immediate environment is induced by the exciton, thereby lowering the exciton energy and causing its localization. In the one-dimensional electronic systems this kind of

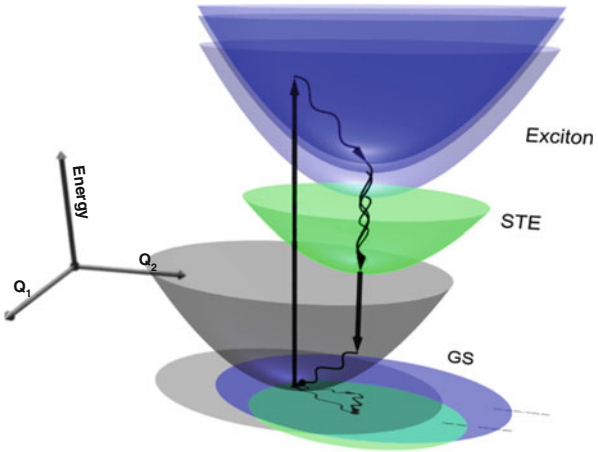


Fig. 2.9 The configuration coordinate model with two (off-diagonal Q1 and diagonal Q2) interaction coordinates for the excitons in the B850 aggregate of LH2. The colored surfaces counted from the bottom of the figure towards the growing potential energy (not in scale) correspond to the ground state (GS, *gray*), self-trapped exciton (STE, *green*), and Frenkel exciton states $k = 0$ and $k = \pm 1$ (Exciton, *blue* of different shades). *Upward* and *downward bold arrows* indicate the photon absorption and fluorescence emission transitions, respectively. The *curly arrows* designate relaxation channels

exciton self-trapping is taking place at all nonvanishing couplings [78], being thus unavoidable in any real structure. The situation is rather different in higher dimensional organizations, where the free and self-trapped excitons, being separated by an energetic barrier, can co-exist. Since the B850 ring can be considered with certain reservations a one-dimensional crystal made from the BChl*a* molecules that strongly couple with their environment, exciton polarons rather than Frenkel excitons are generic photoexcitations of the LH2 antenna complex.

A configuration coordinate diagram (Fig. 2.9) illustrates this issue. Shown in the figure are the adiabatic potential energy surfaces that correspond to the ground state (GS, gray), the three lowest ($k = 0, \pm 1$) light-absorbing Frenkel exciton states (Exciton, blue of different shades), and the relaxed self-trapped exciton state (STE, green). The transitions between the ground and the excited states are linearly coupled via two interaction coordinates. The horizontal Q2 coordinate accounts for the diagonal (energetic) coupling, while the Q1, for the off-diagonal (structural) interaction. The straight and curly arrows represent the optical transitions and relaxation channels, respectively. The reorganization energy related to the diagonal exciton–phonon bath couplings in the LH2 complexes from *Rps. acidophila* is 285 cm^{-1}. The same parameter for the off-diagonal couplings is 73 cm^{-1} [77]. Since just the ground state and the Frenkel exciton states from one side and the self-trapped exciton state and the ground state from another side are directly coupled by photon transitions, it should be clear from Fig. 2.9 that the absorption and emission spectra in such a system deliver different information about the excited states of the matter. While the absorption spectra characterize the exciton

immediately after its creation, the emission spectra describe the exciton behavior immediately before its annihilation [38]. This situation is qualitatively different from that for localized impurities in condensed matter.

2.5.4 *Excitation Energy Dependence of Electron–Phonon Coupling*

As it was already noted above, the basic models ignore possible variations of electron–phonon and/or vibronic couplings, i.e., homogeneous lineshapes, through the IDF. This view is too simplistic, especially for amorphous host materials, where significant dispersion of the solvent shift has been predicted and observed [79, 80]. Strong color effects in the linear electron–phonon coupling strength S [54, 60] were also reported. Figure 2.10 demonstrates a large increase of the Huang–Rhys factor with increasing excitation wavelength across the inhomogeneously broadened absorption band in the low-temperature spectra of glassy samples of Chl*a* and BChl*a* [60, 81]. The observed quasi-linear increase of S suggests a strong correlation between the electron–phonon coupling strength and the solvent shift. Such a correlation can be rationalized within a two-particle Lennard-Jones model of intermolecular interactions [81]. The same model also allows changes of the quadratic couplings, which affect the widths of ZPLs. The latter effect is yet to be shown experimentally.

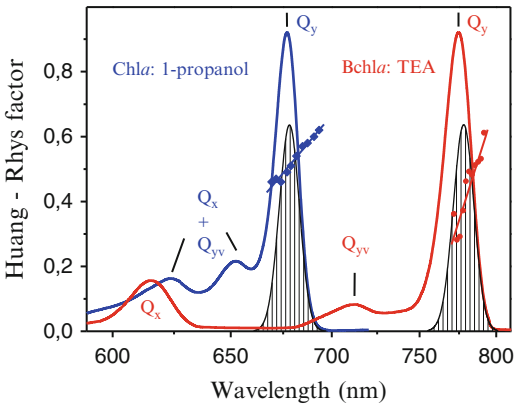


Fig. 2.10 Wavelength dependence of the electron–phonon coupling strength S for the Chl*a*-doped 1-propanol (*blue rhombs*) and for the BChl*a*-doped TEA (*red rings*) solutions at 4.5 K. The lines connecting the scattered data points present linear fits of the data. Plotted on the background with continuous coloured curves are the corresponding absorption spectra. The areas with *drop lines* denote IDF of the ZPL related to the Q_y electronic transitions. A reciprocal (linear in energy) presentation of the wavelength scale is used. Q_y and Q_x refer to the two lowest-energy singlet electronic transitions; Q_{yv} indicates vibronic sidebands related to the Q_y transition

Apparently similar increase of the coupling strength as in Chl*a* and BChl*a* impurity spectra is observed for excitons in the CP29 antenna complex of green plants [54], and the LH2 and LH1 bacterial antenna complexes [73]. While the weakly coupled CP29 excitons in the protein environment are quite expected to act in a similar way as the localized Chl*a* and Bchl*a* molecular excitations in common solvents, the case of strongly coupled as well as self-trapped excitons in bacterial antennas is more complex. A detailed analysis of this situation is beyond the scope of this chapter. We only remark that the latter excitons appear to exhibit strong color effects even without involvement of any solvent shift dispersion [10, 73]. To conclude this paragraph, it is of notice that opposite tendency, i.e., a decrease of S with increasing excitation wavelength, has also been reported in various pigment–protein complexes such as FMO [52] and WSCP [12]. Due to this color effect, the data for the Huang–Rhys factor presented in Table 2.1 are all obtained at the excitation/burn frequency corresponding to the half height of the IDF from the long-wavelength side.

Acknowledgements J. Pieper gratefully acknowledges support by the European Social Fund's Internationalisation Programme DoRa. Furthermore, Estonian Research Council (Grant IUT02-28) and Estonian Science Foundation (Grant No. 9453) supported this work. We are grateful to M. Rätsep, R. Jankowiak, and M. Reppert for stimulating discussions. M. Rätsep and M. Pajusalu designed Figs. 2.5 and 2.9, respectively.

References

1. Frenkel J. Phys Rev. 1931;37:1276.
2. Franck J, Teller E. Migration and photochemical action of excitation energy in crystals. J Chem Phys. 1938;6:861–72.
3. Van Amerongen H, Valkunas L, Van Grondelle R. Photosynthetic excitons. Singapore: World Scientific; 2000.
4. Aartsma TJ, Matysik J, editors. Biophysical techniques in photosynthesis. Dordrecht: Springer; 2008.
5. Jankowiak R, Reppert M, Zazubovich V, Pieper J, Reinot T. Chem Rev. 2011;111(8):4546.
6. Osadko IS. Selective spectroscopy of single molecules. Berlin: Springer; 2003.
7. Ishizaki A, Calhoun TR, Schlau-Cohen GS, Fleming GR. Phys Chem Chem Phys. 2010;12:7319.
8. Müh F, Madjet ME, Renger T. J Phys Chem B. 2010;114:13517.
9. Novoderezhkin V, van Grondelle R. Phys Chem Chem Phys. 2006;8:793–807.
10. Freiberg A, Trinkunas G. In: Laisk A, Nedbal L, Govindjee, editors. Photosynthesis in silico: understanding complexity from molecules to ecosystems. Netherlands: Springer; 2009. p. 55–82.
11. Rebane KK. Impurity spectra of solids. New York: Plenum Press; 1970.
12. Pieper J, Rätsep M, Trostmann I, Paulsen H, Renger G, Freiberg A. J Phys Chem B. 2011;115 (14):4042.
13. Davydov AS. Theory of molecular excitons. NewYork: Plenum Press; 1971.
14. Kühn O, Renger T, May V, Voigt J, Pullerits T, Sundström V. Trends Photochem Photobiol. 1997;4:213.
15. Pieper J, Rätsep M, Trostmann I, Schmitt F-J, Theiss C, Paulsen H, Freiberg A, Renger G. J Phys Chem B. 2011;115(14):4053.

16. Gorokhovskii AA, Kaarli RK, Rebane LA. J Exp Theor Phys Lett. 1974;20:216.
17. Kharlamov BM, Personov RI, Bykovskaya LA. Opt Commun. 1974;12:191.
18. Szabo A. Phys Rev Lett. 1970;25:924.
19. Jaaniso R. Proc Acad Sci Estonian SSR Phys Math. 1985;34:277.
20. Fünfschilling J, Glatz D, Zschokke-Gränacher I. J Lumin. 1986;36:85.
21. Rätsep M, Freiberg A. Chem Phys Lett. 2003;377:371.
22. Moerner WE, Kador L. Phys Rev Lett. 1989;62:2535.
23. Cogdell RJ, Gall A, Köhler J. Quart Rev Biophys. 2006;39:227.
24. Osadko IS. Sov Phys Usp. 1979;22:311.
25. Osadko IS. Theory of light absorption and emission. In: Agranovich VM, Hochstrasser RM, editors. Spectroscopy and excitation dynamics of condensed molecular systems. Amsterdam: Elsevier/North-Holland; 1983. p. 437–512.
26. Hayes JM, Lyle PA, Small GJ. J Phys Chem. 1994;98:7337.
27. Hayes JM, Gillie JK, Tang D, Small GJ. Biochim Biophys Acta. 1988;932:287.
28. Lax M. J Chem Phys. 1952;20:1752.
29. Smith JC. Q Rev Biophys. 1991;24(3):227–91.
30. Orecchini A, Paciaroni A, Bizzarri AR, Cannistraro S. J Phys Chem B. 2002;106:12150.
31. Pieper J, Irrgang K-D, Renger G, Lechner RE. J Phys Chem B. 2004;108:10556.
32. Kurkal V, Smith JC. J Am Chem Soc. 2006;128:2356.
33. Pieper J, Trapp M, Skomorokhov A, Natkaniec I, Peters J, Renger G. Temperature dependent vibrational and conformational dynamics of photosystem II membrane fragments from spinach investigated by elastic and inelastic neutron scattering. Biochim Biophys Acta. 2012;1817:1213.
34. Renger T, Klinger A, Steinecker F, Schmidt am Busch M, Numata J, Müh F. J Phys Chem B. 2012;116:14565.
35. Hochstrasser RM, Prasad PN. J Chem Phys. 1972;56:2814.
36. Hanson DM. Chem Phys Lett. 1976;43:217.
37. May V, Kühn O. Charge and energy transfer dynamics in molecular systems. Berlin: Wiley-VCH; 2000.
38. Toyozawa Y. Optical processes in solids. Cambridge: Cambridge Univ. Press; 2003. p. 149–91.
39. Lu N, Mukamel S. J Chem Phys B. 1991;95:1588.
40. Renger T, Marcus RA. J Chem Phys. 2002;116(22):9997.
41. Kelley AM. J Chem Phys. 2003;119:3320.
42. Laisk A, Nedbal L, Govindjee, editors. Photosynthesis in silico. Understanding complexity from molecules to ecosystems. Heidelberg: Springer; 2009
43. Olbrich C, Jansen TLC, Liebers JR, Aghtar M, Strümpfer J, Schulten K, Knoester J, Kleinekathöfer U. J Phys Chem B. 2011;115:8609.
44. van Oijen AM, Ketelaars M, Köhler J, Aartsma TJ, Schmidt J. Science. 1999;285:400–2.
45. Tietz C, Cheklov O, Dräbenstedt A, Schuster J, Wrachtrup J. J Phys Chem B. 1999;103:6328.
46. Hofmann C, Michel H, van Heel M, Köhler J. Phys Rev Lett. 2005;94:195501.
47. Brecht M, Studier H, Radics V, Nieder JB, Bittl R. J Am Chem Soc. 2008;130:17487.
48. Kunz R, Timpmann K, Southall J, Cogdell RJ, Freiberg A, Köhler J. Single-molecule spectroscopy unmasks the lowest exciton state of the B850 assembly in LH2 from Rps. Acidophila. Biophys J. 2014;106:2008–16.
49. Pieper J, Rätsep M, Jankowiak R, Irrgang K-D, Voigt J, Renger G, Small GJ. J Phys Chem A. 1999;103:2412.
50. Pieper J, Schödel R, Irrgang K-D, Voigt J, Renger G. J Phys Chem B. 2001;105:7115.
51. Pieper J, Voigt J, Renger G, Small GJ. Chem Phys Lett. 1999;310:296.
52. Rätsep M, Freiberg A. J Lumin. 2007;127:251.
53. Reppert M, Naibo V, Jankowiak R. Chem Phys. 2010;367:27.
54. Rätsep M, Pieper J, Irrgang KD, Freiberg A. J Phys Chem B. 2008;112:110.
55. Blankenship RE. Molecular mechanisms of photosynthesis. Oxford: Blackwell Science; 2002.

56. Grimm B, Porra RJ, Rüdiger W, Scheer H, editors. Chlorophylls and bacteriochlorophylls. Dordrecht: Springer; 2006.
57. Renge I, Mauring K. Spectrochim Acta A: Mol Biomol Spectros. 2013;102:301.
58. Avarmaa RA, Rebane KK. Spectrochim Acta A. 1985;41:1365.
59. Lakowicz JR. Principles of fluorescence spectroscopy. New York: Springer; 2010.
60. Rätsep M, Linnanto J, Freiberg A. J Chem Phys. 2009;130:194501.
61. Rätsep M, Cai Z-L, Reimers JR, Freiberg A. J Chem Phys. 2011;134:024506.
62. Dahlbom MG, Reimers JR. Mol Phys. 2005;103:1057.
63. Naumova NL, Vasil'eva IA, Naumov AV, Osad'ko IS. J Lumin. 2005;111:37.
64. Reimers JR, Cai Z-L, Kobayashi R, Rätsep M, Freiberg A, Krausz E. Sci Rep. 2013;3:2761.
65. Liu Z, Yan H, Wang K, Kuang T, Zhang J, Gui L, An X, Chang W. Nature. 2004;428:287.
66. Standfuss J, Lamborghini M, Kühlbrandt W, van Scheltinga ACT. EMBO J. 2005;24:919.
67. Gibasiewicz K, Rutkowski M, van Grondelle R. Photosynthetica. 2009;47:232.
68. Peterman EJG, Pullerits T, van Grondelle R, van Amerongen H. J Phys Chem B. 1997;101:4448.
69. Pieper J, Rätsep M, Irrgang K-D, Freiberg A. J Phys Chem B. 2009;113:10870.
70. Timpmann K, Katiliene Z, Woodbury N, Freiberg A. J Phys Chem B. 2001;105:12223.
71. Freiberg A, Rätsep M, Timpmann K, Trinkunas G, Woodbury NW. J Phys Chem B. 2003;107:11510.
72. Timpmann K, Rätsep M, Hunter CN, Freiberg A. J Phys Chem B. 2004;108:10581.
73. Freiberg A, Rätsep M, Timpmann K, Trinkunas G. Chem Phys. 2009;357:102.
74. Holstein T. Ann Phys. 1959;8:325–42.
75. Heeger AJ, Kivelson S, Schrieffer JR, Su W-P. Rev Mod Phys. 1988;60:781.
76. Trinkunas G, Freiberg A. J Lumin. 2006;119-120:105.
77. Pajusalu M, Rätsep M, Trinkunas G, Freiberg A. Chem Phys Chem. 2011;12:634.
78. Sumi H, Sumi A. J Phys Soc Japan. 1994;63:637.
79. Sesselmann T, Kador L, Richter W, Haarer D. Europhys Lett. 1988;5:361.
80. Kador L, Jahn S, Haarer D, Silbey R. Phys Rev B. 1990;41:12215.
81. Renge I, Rätsep M, Freiberg A. J Lumin. 2011;131:262.
82. Pieper J. Application of high-resolution spectroscopy investigating the energy level structure and electron-phonon-coupling of the light-harvesting complex II of green plants. Ph.D. thesis, Humboldt University Berlin, Berlin, Germany; 2000.
83. Hughes JL, Picorel R, Seibert M, Krausz E. Biochemistry. 2006;45:12345.
84. Dang NC, Zazubovich V, Reppert M, Neupane B, Picorel R, Seibert M, Jankowiak R. J Phys Chem B. 2008;112:9921.
85. den Hartog FTH, Dekker JP, van Grondelle R, Völker S. J Phys Chem B. 1998;102:11007.
86. Neupane B, Dang NC, Acharya K, Reppert M, Zazubovich V, Picorel R, Seibert M, Jankowiak R. J Am Chem Soc. 2010;132:4214.
87. Ihalainen JA, Rätsep M, Jensen PE, Scheller HV, Croce R, Bassi R, Korppi-Tommola JEI, Freiberg A. Red spectral forms of chlorophylls in green plant PS I – a siteselective and high-pressure spectroscopy study. J Phys Chem B. 2003;107:9086–93.
88. Hayes JM, Matsuzaki S, Rätsep M, Small GJ. J Phys Chem B. 2000;104:5625.
89. Chang H-C, Small GJ, Jankowiak R. Chem Phys. 1995;194:323.

http://www.springer.com/978-1-4939-1147-9

The Biophysics of Photosynthesis
Golbeck, J.; van der Est, A. (Eds.)
2014, XI, 462 p. 122 illus., 76 illus. in color., Hardcover
ISBN: 978-1-4939-1147-9